

Comparison of scrape-off layer turbulence simulations with experiments using a synthetic gas puff imaging diagnostic

D. A. Russell,^{1,a)} J. R. Myra,¹ D. A. D'Ippolito,¹ T. L. Munsat,² Y. Sechrest,² R. J. Maqueda,³ D. P. Stotler,³ S. J. Zweben,³ and The NSTX Team³

¹Lodestar Research Corporation, 2400 Central Ave., P-5, Boulder, Colorado 80301, USA

²Department of Physics, Center for Integrated Plasma Studies, University of Colorado, Boulder, Colorado 80309, USA

³Princeton Plasma Physics Laboratory, P.O. Box 451, Princeton, New Jersey 08540, USA

(Received 8 September 2010; accepted 12 January 2011; published online 9 February 2011)

A synthetic gas puff imaging (GPI) diagnostic has been added to the scrape-off layer turbulence (SOLT) simulation code, enabling comparisons with GPI data from the National Spherical Torus Experiment (NSTX) [M. Ono *et al.*, Nucl. Fusion **40**, 557 (2000)]. The edge and scrape-off layer are modeled in the radial and poloidal (bidirectional) dimensions of the outboard midplane region of NSTX. A low-confinement mode discharge is simulated by choosing reference parameters, including radial density and temperature profiles, to be consistent with those of the shot (no. 112825). NSTX and simulation GPI data are submitted to identical analyses. It is demonstrated that the level of turbulent fluctuations in the simulation may be adjusted to give synthetic GPI radial intensity profiles similar to those of the experiment; for a “best-case” simulation, SOLT and NSTX probability distribution functions of blob radial locations, widths, and GPI image velocities are compared. For the simulation, synthetic GPI image velocity and fluid convection ($\mathbf{E} \times \mathbf{B}$) velocity are compared and contrasted. © 2011 American Institute of Physics. [doi:10.1063/1.3553024]

I. INTRODUCTION

Edge and scrape-off-layer (SOL) turbulence has received a great deal of attention in the magnetic fusion community for many decades. Experimentally, the boundary region is relatively accessible to diagnostics and there is a rich variety of edge turbulence data, as reviewed, for example, in Ref. 1. A number of recent papers^{2–8} have also compared the predictions of simulation codes with edge turbulence data. The analysis in Ref. 2 is similar in approach to the present work.

Motivation for this interest comes largely from the fact that the boundary region (edge and SOL) is where the fusion-grade plasma must ultimately interface with material surfaces. It is well known that reducing the heat flux impacting these material surfaces to nondamaging levels is a major constraint on future tokamaks.⁹ Furthermore, the interaction of plasma with surfaces causes recycling of neutrals, which fuel the edge region, impacting the particle balance. Sputtering of impurities into the plasma and wall erosion are also concerns.

It is generally believed that cross-field plasma transport in the SOL is mediated by turbulence. Moreover, early experimental observations,¹⁰ more recent data,^{11–19} and theoretical models^{20,21} suggest that a significant fraction of the turbulent transport is itself mediated by coherent structures, in the form of filaments, often called blob-filaments or simply blobs.

The study of blobs has advanced substantially with the development of fast high resolution imaging cameras (capable of frame rates on the microsecond timescale at thousands of points spatially) together with the gas puff imaging

(GPI) diagnostic technique.^{11,12,22} The GPI diagnostic has enabled a dramatic and direct visualization of plasma convection and cross-field transport by filamentary structures; however, to date, there has been very little quantitative comparison of blob theory with experimental data.

One of the reasons for the apparent difficulty in comparing theory and experiment for blob characteristics (e.g., speed, size, and statistics versus radius) is the inherently statistical nature of turbulence. To circumvent this issue, in the present paper we employ a reduced-model edge turbulence code to simulate both the statistical properties and more deterministic propagation aspects of blob motion. Our goal is a more direct and quantitative comparison of experimental data with theory (i.e., simulation through the solution of equations describing boundary turbulence and blob physics) than has been possible in previous analyses.²³

Important for the sought-after validation of the edge/SOL physics models presently employed is the use of synthetic diagnostics. In the present work, we employ a synthetic GPI diagnostic to simulate the intensity patterns of emission by the turbulent structures. An optical flow diagnostic developed in a separate effort²⁴ is applied to both experimental and synthetic GPI images to enable a direct quantitative comparison of the model and experiment.

Since the focus of the present work is on the modeling of blob dynamics, we choose a low-confinement mode (L-mode) discharge on the National Spherical Torus Experiment²⁵ (NSTX) for our study. In NSTX, L-mode discharges eject copious blobs into the SOL, providing good data for the study of blob speeds and statistics in both the near and far SOL. A study of the near-SOL heat flux width in NSTX high-confinement mode (H-mode) discharges will be presented elsewhere.²⁶

^{a)}Electronic mail: dave@lodestar.com.

The plan of our paper is as follows. In Sec. II we describe the simulation model and an overview of its physics content. Section III gives the simulation parameters and presents an overview of the turbulence for the particular experimental shot under consideration. In Sec. IV the synthetic GPI diagnostic is discussed in detail and results for the two-dimensional (2D) images of turbulence and the radial profiles of various statistical quantities are given. Simulation and experimental results are compared directly. Section V deals specifically with the characteristics of blobs including their number, size, and velocity distributions. Finally, our results are summarized in Sec. VI.

II. SIMULATION MODEL

The 2D scrape-off layer turbulence (SOLT) code simulates turbulence driven by magnetic curvature and drift-wave effects in a 2D plane normal to the magnetic field \mathbf{B} . The simulation domain is the outer midplane of the tokamak, encompassing both the edge and SOL regions. The model includes the effects of wave-phase directionality (drift waves and background flows), curvature drive, radial transport (turbulent Reynolds stress and blobs), sheared flows, and dissipation (sheath loss and friction). A zonally averaged momentum conservation law is used to advance the zonal flows. The physics of the model is described in more detail and a derivation of the equations is provided in a previous paper.²⁷

The code uses local coordinates (x , y , z) for the radial, binormal (approximately poloidal), and parallel directions, where $x \equiv \Delta r = r - r_s$ is the radial distance from the nominal last closed surface, defined at the outer midplane with $\Delta r > 0$ in the SOL. We use x and Δr interchangeably.

The SOLT code evolves dimensionless equations for the electron density n , electron temperature T , vorticity $\nabla^2 \tilde{\Phi}$ (yielding the fluctuating potential $\tilde{\Phi}$), and the zonally averaged poloidal momentum $p_y = (n \cdot v_y)$, derived by integrating the fundamental conservation relations along the magnetic field and using model closures for the parallel physics.²⁸ These four field quantities evolve according to the following equations:

$$\frac{dn}{dt} = \alpha_{dw} \bar{T}^{3/2} \{ \Phi - T \ln n \} - \alpha_{sh} n T^{1/2} e^{(\Phi_B - \Phi)/T} + D \nabla^2 n + S_n, \quad (1)$$

$$\frac{dT}{dt} = -\alpha_{sh} S_E T^{3/2} e^{(\Phi_B - \Phi)/T} + S_T, \quad (2)$$

$$\frac{\partial}{\partial t} \nabla^2 \tilde{\Phi} + \{ \mathbf{v} \cdot \nabla \nabla^2 \Phi \} = \left\{ \begin{aligned} & \alpha_{dw} \frac{\bar{T}^{3/2}}{n} (\Phi - T \ln n) + \alpha_{sh} T^{1/2} (1 - e^{(\Phi_B - \Phi)/T}) \\ & - \frac{\beta}{n} \frac{\partial(nT)}{\partial y} + \mu \nabla^4 \Phi \end{aligned} \right\}, \quad (3)$$

$$\frac{\partial p_y}{\partial t} + \frac{\partial}{\partial x} \langle n v_x v_y \rangle = - \int_x^{L_x} dx \alpha_{sh} \langle n T^{1/2} (1 - e^{(\Phi_B - \Phi)/T}) \rangle + \bar{\mu} \frac{\partial^2}{\partial x^2} \bar{v}_y - \nu_p p_y, \quad (4)$$

where $d/dt = \partial/\partial t + \mathbf{v} \cdot \nabla$ and $\mathbf{v} = \mathbf{e}_z \times \nabla \Phi$ describes convection in the constant background magnetic field $\mathbf{B} = B \mathbf{e}_z$. Here, $\bar{Q} \equiv \langle Q \rangle \equiv \int dy Q / \int dy$ is the zonally averaged piece and $\tilde{Q} \equiv \{Q\} = Q - \bar{Q}$ is the fluctuating piece of Q (note the dual notation). It should be emphasized that Eqs. (3) and (4), with α_{dw} , β , μ , $\bar{\mu}$, and ν_p set to zero, are just the statement of charge conservation, separated into zonally averaged and fluctuating parts (see the Appendix for further discussion of this point). Also note the diffusion operator in the density evolution equation, included to ensure that grid-scale fluctuations in low density regions do not pass through zero, particularly in transient response to initial conditions that are far from equilibrium. (Note the division by density n in various terms of the equations.)

In Eqs. (1)–(4) and throughout the remainder of the paper, we employ dimensionless (Bohm) units

$$\Omega t \rightarrow t, \quad \mathbf{x} / \rho_s \rightarrow \mathbf{x},$$

$$n/n_{ref} \rightarrow n, \quad T/T_{ref} \rightarrow T, \quad \text{and}$$

$$e\Phi/T_{ref} \rightarrow \Phi,$$

where $\Omega = ZeB/m_i c$, $\rho_s = c_s / \Omega$ with $c_s^2 = T_{ref} / m_i$, and n_{ref} and T_{ref} are reference values of the density and electron temperature, specified subsequently, and do not evolve in time. The dimensionless electron adiabaticity parameter α_{dw} , sheath conductivity α_{sh} , and curvature drive β are defined by

$$\alpha_{dw} = \frac{2\rho_s m_i c_s}{L_{||e}^2 \nu_{ei0} m_e}, \quad \alpha_{sh} = \frac{2\rho_s}{L_{||s}}, \quad \text{and} \quad \beta = \frac{2\rho_s}{R}, \quad (5)$$

where ν_{ei0} is a typical value of the electron-ion collision frequency and in Eq. (5) all quantities are evaluated at T_{ref} .

The terms involving α_{dw} in Eqs. (1) and (3) model the electron response (i.e., the parallel current) on closed surfaces; taking α_{dw} large enforces adiabatic electrons. Note that the zonal average of these terms vanishes. The quantity $L_{||e}$ is an effective parallel length scale for electron dynamics inside the last closed surface (LCS), usually taken as the connection length $L_{||} \sim qR$, where q is the safety factor and R the major radius of the torus. We take $\alpha_{dw} = \alpha_{dw}(x)$ to decay rapidly near the separatrix, reflecting the strong increase in collisionality and connection length in crossing the separatrix.

In the SOL, the electron response is modeled by the α_{sh} terms, where $\alpha_{sh}(x)$ vanishes in the core and $L_{||s}$ is the parallel connection length in the SOL to the sheaths. The α_{sh} terms in Eqs. (1)–(4) represent the sheath end loss for particles, energy, charge, and perpendicular momentum. As emphasized in our earlier work,²⁸ the sheath dissipation term in the zonal momentum equation²⁹ is necessary to allow a spontaneous generation of perpendicular momentum in the core. We use the full exponential form of the sheath dissipation terms, valid for arbitrary Φ/T . The Bohm potential

used in this term is given by $\Phi_B = T \ln v \approx 3 T$, where $v = (m_i/2\pi m_e)^{1/2}$. In Eq. (2), s_E denotes the sheath energy transmission coefficient.

The field-line-integrated curvature drive is modeled by the β term. This ‘‘curvature drive’’ is present only in the vorticity equation where it competes with other terms in that equation. The curvature terms that would be present in the density and temperature equations cannot compete with other terms retained in those equations in the tokamak ordering ($L_n/R \ll 1$) and so are absent *ab initio* from the model. This point is discussed in more detail in the Appendix of Ref. 27 and in the Appendix of the present paper.

The model thus incorporates elements of the classical drift-wave model of Wakatani–Hasegawa³⁰ (α_{dw}) in the edge plasma and the blob model equations²⁰ (α_{sh} and β), describing convective transport in the SOL plasma. Note that Eq. (4) preserves momentum conservation for the zonally averaged flows, i.e., it does not use the Boussinesq approximation that is used in Eq. (3). The issue of energy conservation is discussed in the Appendix, where it is shown that the SOL is dominated by end loss to the sheaths and energy need not be conserved.

The dissipation terms involve the following dimensionless coefficients: diffusion D , viscosity coefficients μ and $\bar{\mu}$, and flow damping ν_p . For cool plasmas and high neutral background densities (such as in small scale experiments or near the tokamak divertor plates), ν_p is due to ion-neutral collisions. A study of the turbulence as a function of ν_p was presented in Ref. 27.

The particle and heat source terms are

$$S_n(x) = \nu_n(x)[n_0(x) - n] \quad \text{and} \quad S_T(x) = \nu_T(x)[T_0(x) - T], \quad (6)$$

where $\nu_n(x)$ and $\nu_T(x)$ are tanh-like step functions which vanish in the SOL, thereby defining the LCS. In the limit of large ν_n and ν_T , the profiles are clamped in the edge, i.e., $n \rightarrow n_0(x)$ and $T \rightarrow T_0(x)$, but are free to fully evolve in the SOL. Here, $n_0(x)$ and $T_0(x)$ are reference profiles for the electron density and temperature (see Fig. 1).

Thus, the simulation domain contains two radial regions defined by the source and sink profiles (see Fig. 1 of Ref. 27): (i) the *edge* region inside the separatrix ($\Delta r < 0$) is characterized by nonzero particle, energy source profiles, and drift-wave physics, where $\alpha_{dw}(x)$ is finite; (ii) the *far SOL* ($\Delta r > 5$ cm) is defined by a finite sheath conductivity profile $\alpha_{sh}(x)$. There is an intermediate region (*near SOL*) where both α_{dw} and α_{sh} are small; this simulates the region near the separatrix, where the parallel connection length is long ($L_{\parallel} \propto 1/\alpha_{sh} \rightarrow \infty$). The left boundary of the simulation represents the matching of the edge to the core plasma and the right boundary represents the location of the wall bounding the SOL plasma.

Our computational model is similar to the one used by Bisai *et al.*³¹ with two additional features. We evolve the electron temperature and we use a separate momentum conserving equation to evolve the y -momentum. It is also

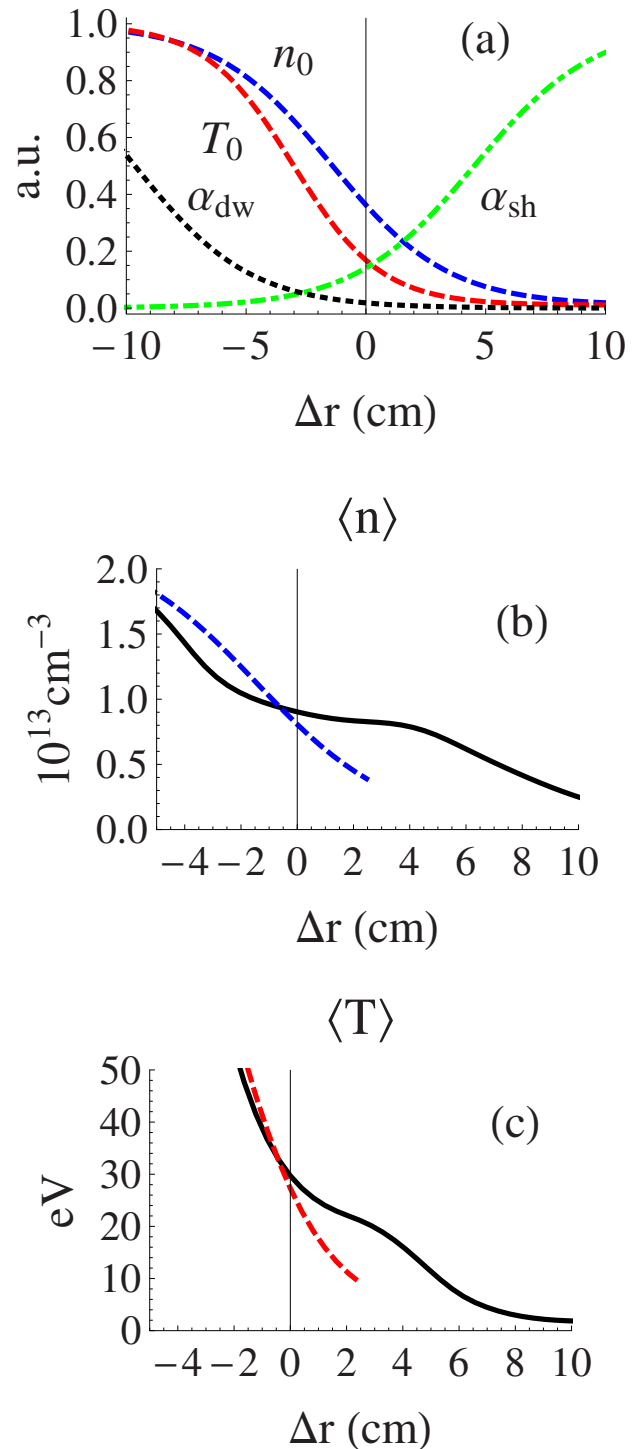


FIG. 1. (Color online) (a) α_{dw} and α_{sh} parameter profiles, with reference density (n_0) and temperature (T_0) profiles that were fitted to Thomson scattering data from NSTX shot no. 112825 for the simulations, all normalized by their maxima. (b) Density and (c) temperature profiles from a SOLT simulation ($\beta = 1.75 \times \beta_0$) are shown with fragments of the corresponding reference profiles in (a). Δr is the distance from the magnetic separatrix in the experiment, with positive values corresponding to the SOL. $\langle \dots \rangle$ denotes averaging over y and t .

similar to the model used in the ESEL code,³² the main differences being that SOLT retains additional drift-wave physics in the edge plasma and the full exponential form of the sheath term in the SOL.

III. SIMULATION PARAMETERS AND PROFILES OF THE TURBULENCE

The physical parameters for the SOLT simulations were chosen to be consistent with NSTX shot no. 112825,²³ a low-confinement mode discharge in a deuterium plasma. The simulation used the following outboard midplane parameters: $B=2500$ G, $R=150$ cm, $\rho_s=0.52$ cm, $n_{\text{ref}}=10^{13}$ cm⁻³, $n_{\text{wall}}=2 \times 10^{11}$ cm⁻³, $T_{\text{ref}}=82$ eV, $T_{\text{wall}}=1.7$ eV, and $c_s=63$ km/s; and dimensionless parameters: $\alpha_{\text{DW}}=0.11$, $\alpha_{\text{sh}}=2 \times 10^{-3}$, $\beta_0=2\rho_s/R=7 \times 10^{-3}$, $\mu=0.1$, $\bar{\mu}=0.01$, $D=0.01$, and $s_E=6$. Reference density and temperature profiles $[n_0(x)$ and $T_0(x)$ in Eqs. (6)] were chosen to match the measured Thomson profiles in the near-edge region by least-squares fit to hyperbolic tangent functions (see Fig. 1). The dimensionless source rates ν_n and ν_T [Eqs. (6)] are similar in shape to their corresponding reference profiles and reach maxima ($x \rightarrow -\infty$) of 0.01 and 0.1, respectively. [The reference values of density and temperature lie on the core side of the separatrix ($\Delta r < 0$) at the inflection points of the tanh functions.] The reference profiles and source rates are exponentially small in the far SOL. These values of ν_n and ν_T are somewhat arbitrary though they set source function parameters that are intended to model restoration (e.g., refilling of holes left in the core) by parallel transport, ionization sources, etc. Clearly too small a restoration rate leads to departure from the core profiles of the shot and too large a rate can quench the turbulence; we have not investigated these dependencies in detail.

The flow damping parameter ν_p is set equal to zero in these simulations. In a previous study,²⁷ we found that this choice gave the best qualitative agreement with L-mode turbulence on NSTX, i.e., production of blobs and not radially extended streamers, due to the effect of zonal flow shear layers in the simulations.

In general, the simulation results can be very sensitive to changes in the driving and damping parameters, as demonstrated in Ref. 27, where order-unity changes in the zonal flow damping parameter alone led to dramatic qualitative changes in the character of the turbulence. The sensitivity of this rich model to both changes in its parameters and to perturbations in the form of the equations, particularly the functional forms of SOL dissipation terms and of imposed zonal flows, is central to our ongoing validation program, featuring the present study as an important milestone.

Experience with a large number of SOLT code runs has shown that L-mode turbulence in the experiments results in instability drives that are in a delicate balance with dissipation and zonal flows. Because the balance is rather sensitive, it is usual that some modest tuning of initial input parameters is required for realistic simulations (i.e., to avoid the extremes of quiescence or an overly violent edge, neither of which is observed). In this study, we have chosen to hold fixed the dissipation parameters, which are not directly measured in the experiment, and to tune the strength of the turbulence by changing the curvature drive strength β consistent with uncertainties inherent in applying the present 2D model to the NSTX edge plasma (e.g., ion and electron pressure-weighted average curvature versus the local out-

board midplane value of β). Since the reference value β_0 happens to be too small to sustain a turbulent state against this dissipation, $\beta > \beta_0$ is chosen in the simulations and we present results for only three choices of β , as noted subsequently, $\beta=2 \times \beta_0$, $\beta=1.75 \times \beta_0$, and $\beta=1.5 \times \beta_0$, focusing our attention exclusively on the intermediate value in Sec. V.

We impose zero fluctuation amplitudes ($\delta\phi$, $\nabla^2\delta\phi$, δn , and δT) at the radial (x) boundaries where the y -averaged, or zonal, density and temperature are fixed at their reference-profile values. For the zonal flow, we take $\bar{\Phi}$ equal to the Bohm potential (3T) at the wall (far-SOL radial boundary) and specify the poloidal flow velocity $\partial_x\bar{\Phi}$ on both boundaries: zero at the wall and $-0.4c_s$ on the core-side boundary. All fields are periodic in y .

We have experimented with other boundary conditions for the zonal flow, including holding the potential fixed while allowing the velocity to evolve freely on the core-side boundary. In that case, the properties of the turbulence in the near-edge and SOL are similar to the fixed-velocity cases presented here, all other parameters being equal, but the zonal velocity on the core-side boundary continues to decrease through negative values, apparently without limit, on the relatively long diffusive time scale set by $\bar{\mu}$. Since we make no attempt to model transport in the core accurately, we hold the zonal velocity fixed on the core-side boundary. The value chosen is typical of the open boundary condition cases observed after similar run times (2.5 ms).

The simulation box size is $(L_x, L_y)=(100, 100)$ ρ_s on a 128×128 grid. Spot-checking with higher-resolution and larger-in- y simulations suggests that this size and resolution are adequate for the driving and damping parameters explored here.

Time-averaged and y -averaged radial profiles of saturated-state turbulence for three drive strengths (β) are shown in Fig. 2. The expected behavior is obtained,²⁷ with increasing drive strength, radial particle and heat²⁶ fluxes increase, bulging profiles of density and temperature into the SOL. Radial particle flux peaks at $\Delta r \cong 0$, near the maximum linear growth rate for the reference profiles.

The simulations are characterized by persistent, downward (in the $-y$ direction) zonal flows that are largely established early in the simulations by the $E \times B$ drift associated with the Bohm potential (3Te) at the entrance to the sheath. By zonal flow (ZF), we mean the y -averaged y -component of the fluid velocity $\langle v_y \rangle_y(x, t)$, obtained from the solution of Eq. (4). The zonal flows, averaged over the last half of the simulations, are plotted in Fig. 2(c) and their radial derivatives, or flow shear, in Fig. 2(d). Notice the local minimum in shear at a negative value ($\cong -80$ kHz) just inside the separatrix and that the stronger the drive β , the more negative the shear at that minimum. This is consistent with the control of the interchange instability by ZF shear expected in these cases of no ZF damping, appropriate for simulating L-mode shots at NSTX.²⁷

Near the local shear minimum, the skewness S_p of plasma pressure fluctuations³³ passes through zero [$\Delta r \cong -3$ cm; see Fig. 2(e)] and increases from negative to positive values with increasing radius. The blob *birth zone* is

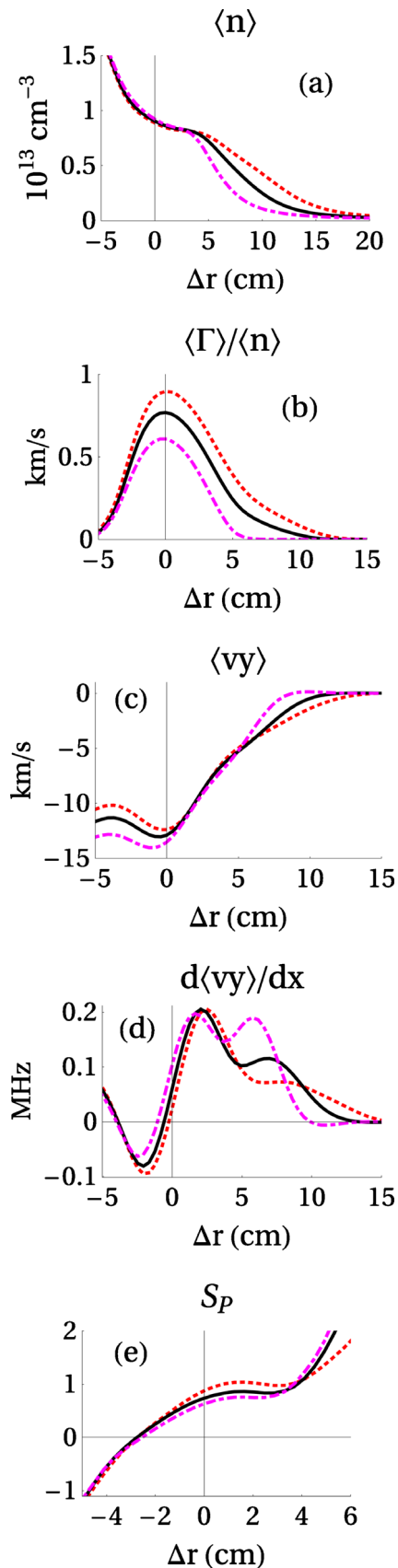


FIG. 2. (Color online) Radial profiles of (a) density and (b) radial particle flux ($\Gamma = n \cdot v_x$) divided by the density profile (a radial convection velocity), (c) zonal flow, (d) zonal flow shear, and (e) the skewness of pressure fluctuations $S_p = \langle (\delta p)^3 \rangle / \langle (\delta p)^2 \rangle^{3/2}$, $\delta p = p - \langle p \rangle$, and $p = n \cdot T$ for the three simulations: $\beta = 2 \times \beta_0$ (dashed, red), $1.75 \times \beta_0$ (solid, black), and $1.5 \times \beta_0$ (dotted-dashed, purple). $\langle \dots \rangle$ denotes averaging over y and t .

centered where $S_p = 0$;³⁴ positive fluctuations (blobs) move radially outward from this location and negative fluctuations (holes) move inward. Between the birth zone and the *sheath entrance* [where α_{sh} increases most rapidly ($\Delta r \cong 4.5$ cm), corresponding approximately to the location of the rf limiter in NSTX], the skewness increases and eventually plateaus near unity, as intermittently emitted blobs increasingly dominate the turbulent fluctuations. Beyond the sheath entrance, S_p increases dramatically above unity, though the calculation may be suspect owing to the paucity of data in the far SOL.

IV. THE SYNTHETIC GPI DIAGNOSTIC

Since its introduction,^{11,12,23} GPI has given us unprecedented pictures of edge turbulence on NSTX,¹¹ Alcator C-Mod,³⁵ and RFX-Mod.¹³ A puff of neutral gas is injected toward the core from a port in the outboard wall of the machine. Collisions with plasma electrons stimulate atomic emission from the neutrals and the radiation is captured on a charge-coupled device camera. In NSTX, the image window includes several centimeters of the core and much of the SOL plasma. Since the image is effectively a slice perpendicular to the magnetic field, field-aligned cylindrical filaments of plasma appear as round blobs. (For the single discharge examined in this paper, the camera was looking along the magnetic field in the outboard midplane.) Here we construct similar images from the SOLT simulations using a *synthetic* GPI diagnostic. A similar diagnostic was used in Ref. 8 to analyze simulations of a small-fluctuation model that cannot treat blobs.

Density and temperature data from the simulations are converted to a synthetic GPI intensity using the neutral gas puff density profile for the experiment (N_0), obtained from DEGAS-2 (Ref. 36) simulations, and the atomic emission function f_A for the experimentally detected spectral line; for shot no. 112825, the gas puff was helium and the α -line emission (587.6 nm) was recorded. The intensity of emission has been tabulated and is well fitted by

$$I \sim N_0 \cdot f_A(n_e, T_e), \quad (7)$$

where $f_A \sim n_e^\nu T_e^\mu \exp(-E_\alpha/T_e)$, $\nu = 0.76$, $\mu = -1.058$, and $E_\alpha = 28.16$ eV. The constants of proportionality in these expressions are unimportant for our purposes, since we make comparisons between quantities that are independent of the absolute intensity of emission (e.g., skewness of intensity fluctuations) and present both simulated and experimental intensities normalized by their respective means, as noted.

A GPI frame showing a typical blob from NSTX shot no. 112825 and one from a SOLT simulation are shown in Fig. 3. Note that the simulation blob is smooth and poloidally elongated, whereas the experimental blob is smaller and more circular in shape; it has a compound structure that is recorded as multiple blobs by the blob tracking routine. These properties help account for the statistical differences observed in Sec. V below. The SOLT window shown here is a subdomain ($\sim 1/9$) of the full simulation. The line $\Delta r = 0$ coincides with the location of the magnetic separatrix in the

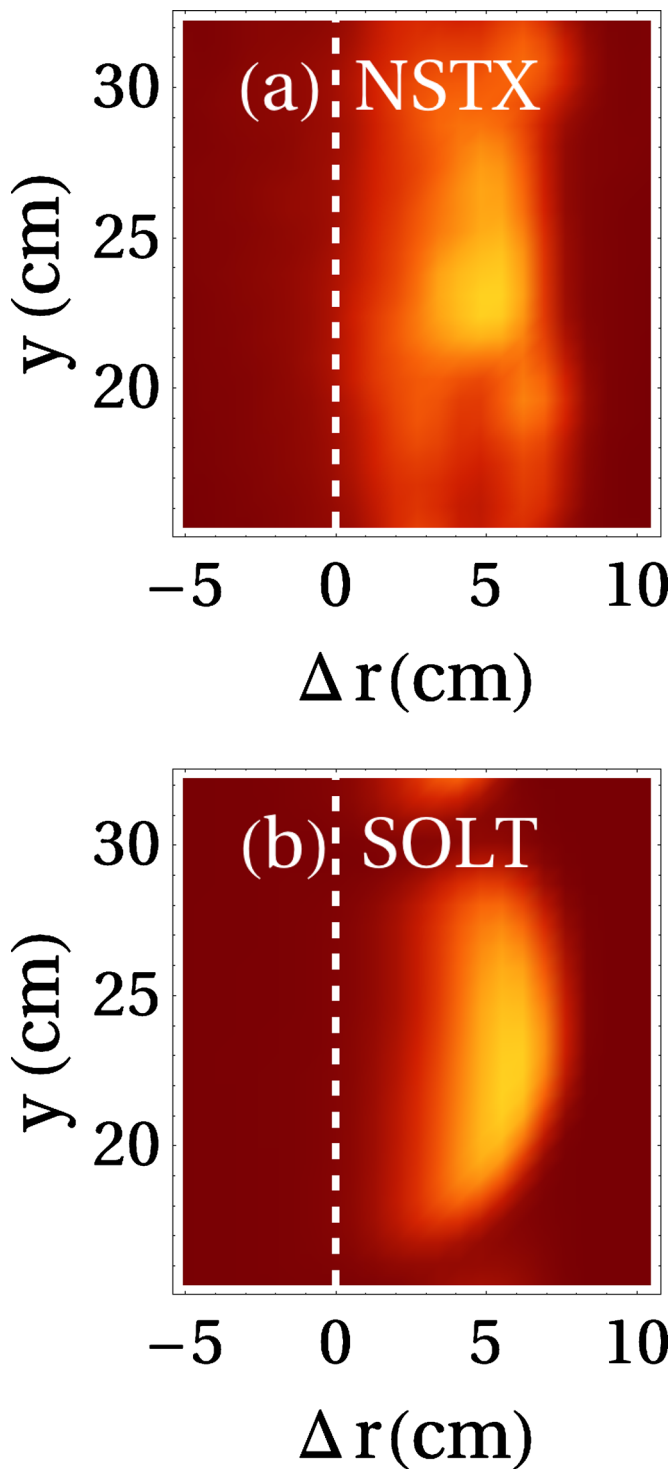


FIG. 3. (Color online) (a) Actual (NSTX, shot no. 112825) and (b) synthetic SOLT GPI intensity images. The magnetic separatrix is at $\Delta r=0$ in the NSTX shot. Intensities are normalized by their respective global maxima over the frame. The SOLT window is a subdomain ($\sim 1/9$) of the full simulation ($\beta=1.75 \times \beta_0$).

shot and is indicated in the experimental n_e and T_e profile data, to which the simulation reference profiles are fitted. We linearly interpolate the synthetic intensity onto a grid corresponding to the camera data and sample it at the same frame interval as in the experiment (4 μ s).

The neutral density profile $N_0(x)$ is a rapidly increasing

function of radius, negligible in the core ($\Delta r < 0$) and curtailed abruptly at the limiter $\Delta r=10.5$ cm. This increase in N_0 enhances blob brightness in the far SOL, despite the loss of blob density and temperature to the divertor in the course of radial propagation.

The absolute intensity of emission from the plasma is not available from the GPI camera data (though it can be calculated, in principle, from the simulation density and temperature). However, telling comparisons of *relative* intensity can be made. For example, the departure of average from median intensity reveals the presence of relatively rare, strong events, i.e., intermittently ejected blobs detected in the far SOL, increasingly apparent with stronger drive strengths (see Fig. 4).

We explored the sensitivity of the model and found that varying β (turbulence level) and the $\alpha_{sh}(x)$ profile ($L_{||}$) gave us a reasonable degree of freedom to match the experimental shot. The distribution of turbulent fluctuations entering the SOL from the edge region is a function of the drive strength β . Given that distribution, the location of the maximum median GPI intensity (and its width) is determined by the neutral density profile and by the sheath absorption profile $\alpha_{sh}(\Delta r)$ (which is uncertain because downstream plasma conditions at the sheath itself are not measured). In the far SOL, intensity diminishes with increasing radius despite increasing neutral density and the GPI intensity grows more intermittent with increasing Δr , starting near the sheath entrance. (The separation of mean from median intensity in Fig. 4 indicates increasing intermittency, consistent with the increase in skewness in the far SOL in Fig. 5.) Since the simulations place the maximum median emission intensities within 1 cm of the corresponding maximum in the shot, it may be inferred that $\alpha_{sh}(\Delta r)$ fairly locates the sudden decrease in parallel connection length with increasing radius in the outboard midplane (as one moves away from the separatrix) for this shot. The width of the emission profile may be similarly fine-tuned to approximate that of the shot.

This crafted agreement [e.g., between Figs. 4(b) and 4(d)] does not establish that we have captured all the physics responsible for the experimental intensity profile with our model of sheath absorption, but it demonstrates the capability to explore that and similar possibilities through GPI comparisons.

For pressure fluctuations in the simulations, the skewness passes through zero in the birth zone of the turbulent fluctuations, as described in Sec. III. The skewness of intensity fluctuations S_I appears to share this property when computed from the experimental data but not from the simulation (see Fig. 5). However, the intensity data for the shot are barely above noise inside the separatrix, due to low neutral density, and it is difficult to ascribe a zero to the skewness there with certainty. More reliable comparisons can be made in the SOL.

In the SOL, S_I is everywhere positive for the shot, while for the simulation, it is negative on the core side of the sheath entrance. All three curves rise to exceed unity where blobs that can survive stronger sheath absorption are increasingly intermittent, beyond the sheath entrance in the far SOL.

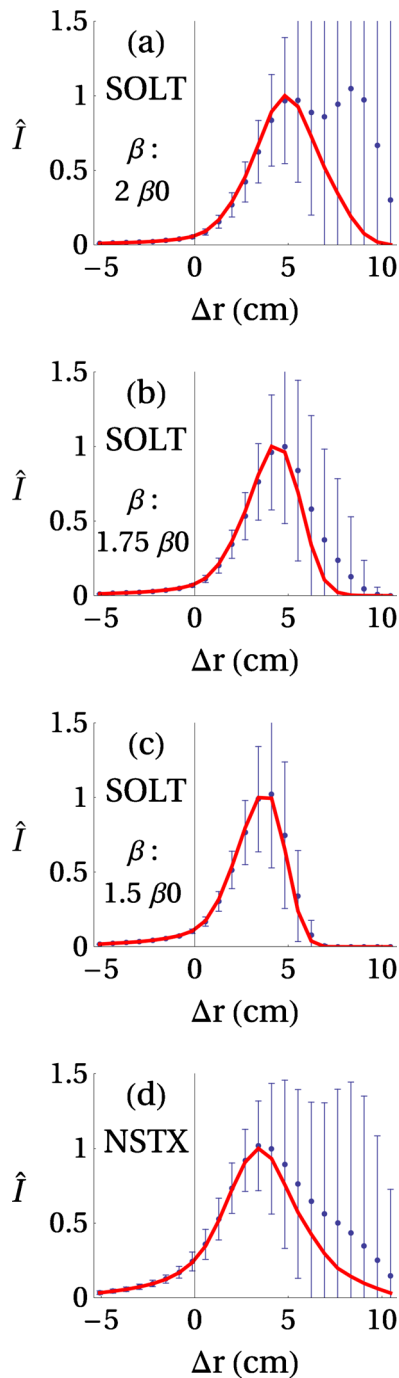


FIG. 4. (Color online) Median (solid, red) and average (dots) GPI intensities, sampled over y and t (300 frames), vs radius for three drive strengths in the SOLT simulations (a) $\beta=2\times\beta_0$, (b) $\beta=1.75\times\beta_0$, and (c) $\beta=1.5\times\beta_0$, compared to (d) the GPI camera data for NSTX shot no. 112528. Error bars denote root-mean-square deviation from the average. All data are normalized to the maximum value of the median in each case.

(This is consistent with the separation of average and median intensity profiles observed in Fig. 4.)

We can offer a possible explanation for why the simulation S_1 is negative in the near SOL. We observe from Fig. 1 that the electron temperature in the near SOL is greater in the simulation than in the experiment. The atomic emission function f_A decreases with increasing T_e for $T_e > E_\alpha$. Thus, temperature fluctuations hotter than E_α (28.16 eV) are anti-

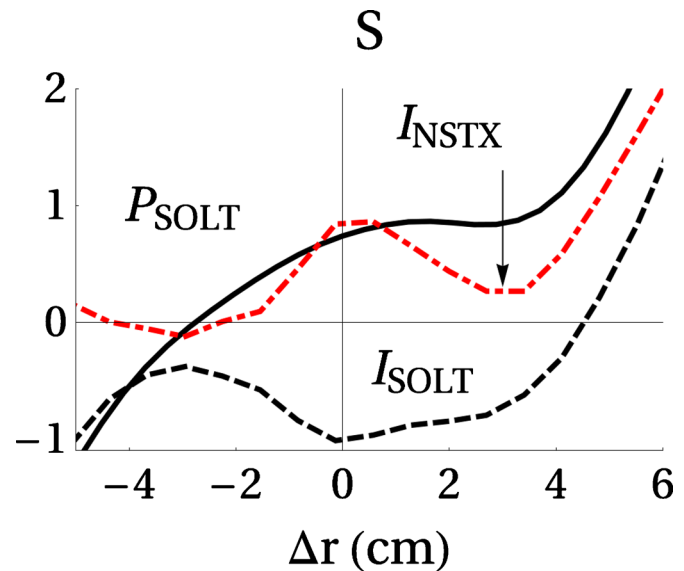


FIG. 5. (Color online) The skewness of pressure fluctuations S_p (solid, black) and of synthetic GPI intensity fluctuations S_1 (dashed, black) vs radius for the SOLT simulation with $\beta=1.75\times\beta_0$. S_1 for the NSTX shot (dashed-dotted, red) is positive for $\Delta r > -2$ cm.

correlated with intensity fluctuations; blobs hotter than E_α tend to make S_1 negative. Indeed, time-averaged temperatures in the near SOL are higher in the simulation than in the experiment [Fig. 1(b)], yet edge temperature and density profiles have been lined up, so blob temperatures and densities are similar at birth. To account for the temperature discrepancy in the SOL, electron energy loss rates may be higher there than we have assumed (such as enhanced sheath losses or energy losses due to impurity radiation).

This section discussed properties of GPI intensity fluctuations gleaned from point measurements, as a function of radial location. The obvious “blobbiness” of the fluctuations in Fig. 3 notwithstanding, no mention of blobs need have been made. Next we compare shot and simulation GPI intensity blobs with respect to radial distribution, width in the poloidal (binormal) dimension, and velocity. We confine our attention hereafter to “the simulation” $\beta=1.75\times\beta_0$. Of the three simulations, the median and average intensity profiles for this case appear to separate, with increasing radius beyond the sheath entrance, most like those of the shot (see Fig. 4).

V. GPI BLOBS

A blob is a poloidally (y) localized excess of plasma pressure in the outboard midplane region of the tokamak.²⁰ About such maxima, the curvature and grad- B drifts induce charge polarization in y and the resulting electric field gives the blob a radially outward $\mathbf{E}\times\mathbf{B}$ drift velocity (\mathbf{v}_E). The charge polarization is described by the β -term in Eq. (1). Previous simulation studies found that such turbulent propagating objects tend to be radially localized blobs in the presence of sheared zonal flows and radially extended streamers absent such flows.²⁷ In the present case of well developed zonal flows in the simulation, the blobs are generally round or poloidally elongated ellipses (Fig. 3).

A blob of plasma registers as a blob of GPI intensity in the SOL. The translation of density and temperature into intensity is provided by Eq. (7). We define a GPI intensity blob, for both experimental and synthetic data, as a local spatial maximum $\partial_x I = \partial_y I = 0$, where the intensity exceeds the instantaneous poloidally averaged intensity $I_{\text{blob}}(x, y, t) > \langle I \rangle_y(x, t)$. We note that this definition of a blob differs from the selection rules often used in experimental data analysis (e.g., keeping only fluctuations that exceed 2.5–3 standard deviations), but we emphasize that the same rule is applied here to both the simulation and the experimental data. The restriction to radial maxima tends to eliminate the trailing tail of the blobs from consideration. Raising the amplitude threshold reduces the noisy background of relatively short-lived fluctuations (e.g., those observed at low, occasionally negative, radial velocities, found in the wakes of the brighter blobs) in the data sample. This conditional sampling selects objects that have the look and feel of blobs in the GPI pictures, though not all frames yield a blob by this definition. A single blob may make several appearances in successive frames and its properties are recorded in the statistical sample each time it does so.

Because the shot intensity images are noisy on the scale of the original data grid, we smooth them with nearest-neighbor averaging in x and y , reducing the number of grid points per frame by one quarter. The synthetic intensity images are smoothed in exactly the same way before screening both data sets for blobs.

The numbers of intensity blobs discovered in the simulation and in the shot are plotted in Fig. 6(a) as a function of radial location. The blob finder discovers totals of 1087 blobs in the shot and 434 blobs in the simulation, distributed over 300 frames in each case. Note the plateau in the NSTX data, extending into the far SOL, that includes a spike in population at $\Delta r \cong 8$ cm. This plateau may indicate a greater tendency for the NSTX blobs to fragment, slow down with propagation ($dv_x/dt < 0$), or generally linger in the camera window longer than the simulation blobs. (A blob is counted every time it appears in the frame in both experiment and simulation.) The blobs' charge polarization propels it locally, but it swims in the background flow, and it is reasonable to expect differences in the background flows to contribute to differences in blob distributions such as that illustrated in Fig. 6(a).

From the GPI data, it is clear that the zonal flows are very different in the simulation and the experiment. The time-averaged zonal flow profile and its radial derivative (shear) for the simulation are shown in Figs. 2(c) and 2(d). The flow is quasistationary in the simulation, with relative temporal fluctuations not greater than 10%. In the NSTX GPI data, fluctuations are of order-unity: the flow appears to come and go irregularly. Based on theory,^{31,37} blobs are expected to linger between (and fragment in traversing) radial ZF shear layers, as the flow spins up the blob, reducing the blob charge polarization. Occasionally, a NSTX blob will pause before proceeding further into the SOL, as though momentarily entrained between shear layers, acting like “gutter blobs.” Blob entrainment is clearly evident in the simulation and is responsible for the dominant peak in the blob popula-

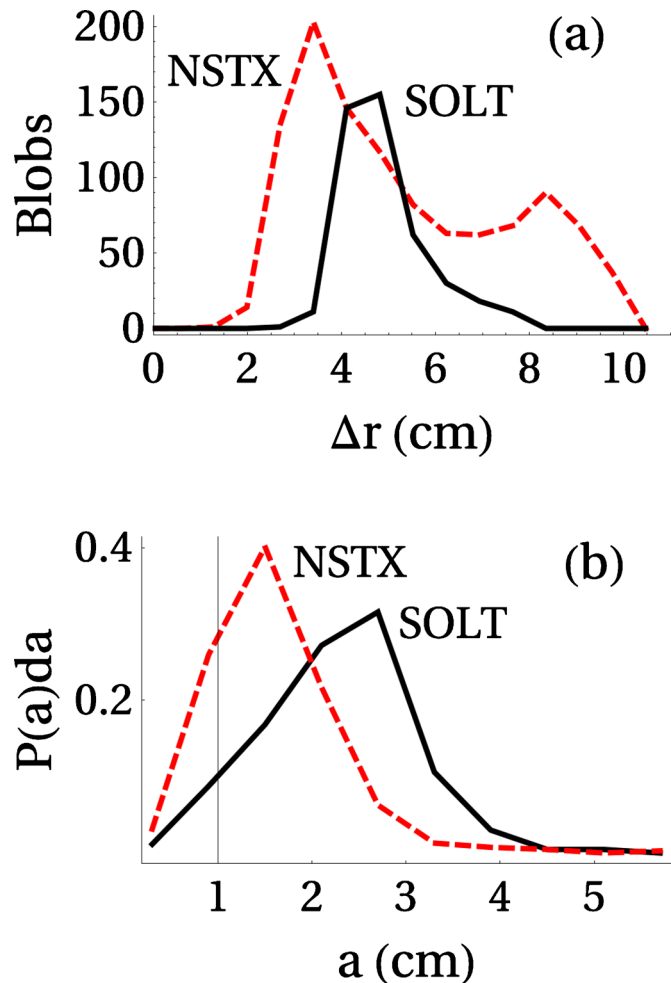


FIG. 6. (Color online) For GPI images in the SOLT simulation ($\beta=1.75 \times \beta_0$, black, solid) and in NSTX shot no. 112825 (red, dashed): (a) the number of intensity blobs detected vs radius and (b) the distribution of intensity-blob poloidal half-widths. All pdfs use ten uniform bins.

tion near the sheath entrance at $\Delta r=4.5$ cm. However, ZFs have not been measured in the NSTX shot under study here, though they are discernable in the GPI movies and their role in blob dynamics in the SOL is a topic of ongoing investigation.

We measure the poloidal width of a blob by varying the width of a Gaussian profile centered on the intensity maximum $I \sim \exp[-(y-y_0)^2/(2a^2)]$ to minimize the mean-square difference with the data over nearby points.³⁸ The distributions of widths for the intensity blobs are plotted in Fig. 6(b).

The SOLT blobs are about twice as wide as the NSTX blobs. Since the near-edge profile gradients determine the blob widths at birth,²⁰ this result may suggest that the SOL diffusion coefficients are larger in the simulation than appropriate for modeling the shot. However, a more likely cause of the disparity in widths is the persistent, broad shear layer in front of the sheath entrance in the simulation that smears the blobs poloidally [see Fig. 2(d)].

The velocity with which density and temperature fluctuations are convected is not necessarily the GPI image velocity in either the simulation or the experiment. (Nor is the $\mathbf{E} \times \mathbf{B}$ convection velocity directly measured by GPI in the

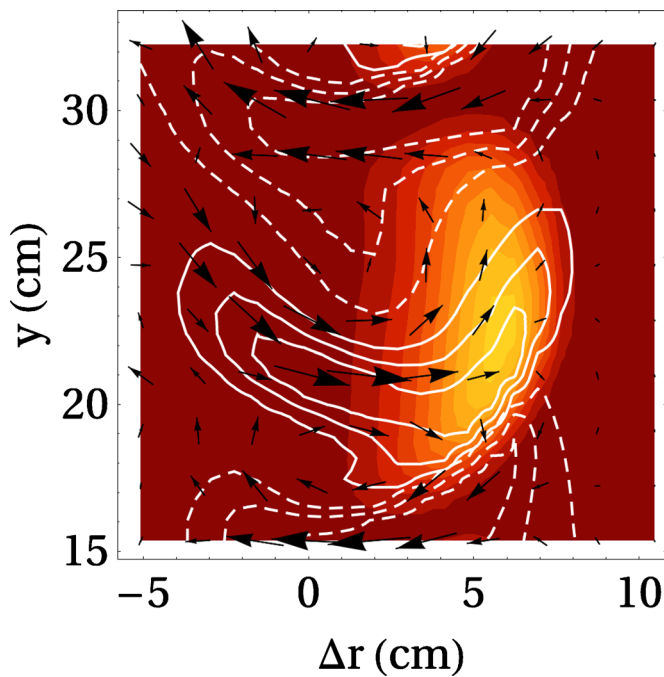


FIG. 7. (Color online) A snapshot of the synthetic GPI intensity blob from the SOLT simulation [Fig. 3(b)] shown with contours of pressure fluctuation, relative to the poloidal average $(p - \langle p \rangle) / \langle p \rangle$ (positive: solid, white; negative: dashed, white) and flow velocities with respect to the local zonal flow $\mathbf{v}_E - \langle \mathbf{v}_E \rangle$ (black arrows). $\langle \dots \rangle$ denotes averaging over y .

experiment.) Within the GPI intensity blob, the underlying convection velocity can be complex, particularly for interacting blobs. But in the textbook case of the isolated, round density blob on a uniform-density background,³⁹ the internal flow is a vorticity dipole. The dipole centers (charge density extrema: $\hat{\mathbf{b}} \cdot \nabla \times \mathbf{v}_E = \nabla^2 \phi$) move at the average velocity and the outer edge is at rest with respect to the ambient plasma (no slip), so the total velocity midway between them, at the center of the pressure blob, is greater than the average by about a factor of 2. There is evidence for this simple dipole picture, even in these strong-turbulent, many-blob simulations with zonal flow (see Fig. 7).

A consequence of the internal flow pattern is that the radial convection velocity $(\mathbf{v}_E)_x$ is maximized, with respect to y , along the spine (i.e., the line of poloidal symmetry) of the simple blob. Thus, one might expect the convection velocity at the intensity maximum (near the spine) to be greater than the image velocity, for example, if the latter were simply a poloidal average over the extent of the blob. In any case, 2D images of $(\mathbf{v}_E)_x$ are unavailable experimentally, so a direct comparison of simulation and experiment requires an analysis of intensity-blob image velocities.

To measure intensity-blob image velocities, a method for extracting velocity flows from the image data set is required. Particle image velocimetry is one such method that has been employed in the literature.⁴⁰ Here, we report on results using the method of *hybrid optical flow and pattern matching velocimetry* (HOP-V), developed to measure GPI image velocities at NSTX.²⁴ HOP-V assigns a velocity field to each GPI frame by (i) solving the intensity continuity equation for an initial approximation to the velocity (the “optical flow”

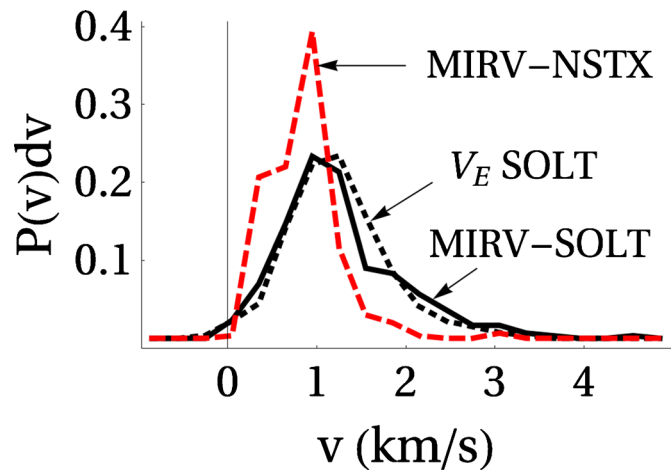


FIG. 8. (Color online) The distribution of the MIRV for the SOLT simulation (solid, black) and for the NSTX shot (dashed, red) and the distribution of the radial convection velocity $(\mathbf{v}_E)_x$, measured at the intensity maximum of the brightest blob in each frame of the SOLT simulation (dotted, black). All pdfs use 20 uniform bins.

method) and (ii) refining the estimate by adjusting a displacement field to maximize a correlation function between successive intensity images (“pattern matching”). The hybrid method overcomes limitations of either method alone when applied to coarsely resolved data. The algorithm has been benchmarked on prescribed flows and images.²⁴

HOP-V sacrifices spatial localization for accurate measurement of high image velocities. Due to the interpolation implicit in HOP-V and the temporal sparseness of the data, the optical velocity at the intensity maximum is a poor measure of the underlying flow at that point. However, the algorithm is particularly sensitive to sudden displacements and accurate at measuring the *maximum* image radial velocity (MIRV) in each frame (even if that velocity is associated with a relatively faint intensity fluctuation).

For the simulation, we plot the MIRV probability distribution function (pdf) and the pdf of the radial component of the convection velocity $(\mathbf{v}_E)_x$ of the brightest blob in each frame, measured at the intensity maximum, in Fig. 8. HOP-V accurately reveals the convection velocity of the brightest blob in the frame because the intensity maximum is moving with the greatest image velocity, on average, consistent with the simple model of internal blob flow and suggested in Fig. 7.

The MIRV pdf for the NSTX shot is also plotted in Fig. 8. The overall agreement between the simulation and NSTX data is gratifying. The mean, standard deviation, and skewness of the (NSTX, SOLT) MIRV distributions are (0.8, 1.2) km/s, (0.4, 0.7) km/s, and (1.6, 1.3), respectively. It is worth noting that the $(\mathbf{v}_E)_x$ measured at the pressure maximum is substantially different (about a factor of 2 larger) from that measured at the intensity maximum (e.g., see Fig. 7). Thus, using a synthetic GPI diagnostic and subjecting both experimental and simulation data to exactly the same analysis procedure (i.e., HOP-V) are important to obtaining the agreement in Fig. 8.

VI. SUMMARY AND DISCUSSION

The SOLT code, which simulates turbulence in the near-edge and scrape-off layer of the outboard midplane, was enhanced with a synthetic GPI diagnostic to enable comparisons with real GPI images from experiments on NSTX. Near-edge profiles of density and temperature in the simulations were lined up with those of NSTX shot no. 112825, measured by Thomson scattering, to create similar conditions in the blob birth zone.

We did a sensitivity study of the model and found that varying β (turbulence level) and the $\alpha_{\text{sh}}(x)$ profile (L_{\parallel}) gave us a reasonable degree of freedom to match the experimental shot. It was suggested that comparisons of radial profiles of median and average (normalized) GPI intensities was the best way to determine the optimal parametrization. This procedure revealed the sensitivity of the turbulence to the effective parallel sheath connection length and the distance of the sheath entrance from the separatrix, i.e., the width of the inertial transport region in the outboard midplane.

With increasing curvature drive β , the level of turbulence increases, as does the separation between average and median intensity profiles in the SOL. A simulation was selected for the resemblance of these profiles to those of the shot (Fig. 4); it may be inferred from this agreement that the chosen simulation and shot have similar intensity fluctuation characteristics, particularly with respect to degree of intermittency, in the SOL. Factor-of-2 agreement between the simulated and experimental number of blobs and size distributions were obtained for the best-case simulations. Furthermore, within experimental and modeling uncertainties, the input parameters for this best-case simulation were well matched to the available experimental data.

To explore and compare the nature of intensity fluctuations beyond the limitations of spatially localized measurements, a simple blob finder was introduced and exercised on the SOLT and NSTX GPI data.

Distributions (pdfs) of the size and velocity of intensity blobs were compared. SOLT blobs are wider poloidally than NSTX blobs, likely due to differences in sheared zonal flows, which tend to be stronger and less intermittent in these simulations. It is conceivable that the ZFs in the experiment cannot be modeled by SOLT without introducing a mechanism for strongly perturbing the zonal momentum (p_y) away from its long-time course of evolution as self-consistently modeled in SOLT at present, e.g., by changing the ZF boundary conditions in the course of the simulation or simply by legislating the observed experimental ZF. This is a subject of ongoing study.⁴¹

The distinction between fluid convection velocity (\mathbf{v}_E)_x and image velocity was elaborated. Applying a proven image velocimetry algorithm (HOP-V) to the SOLT intensity blobs, we found pdfs of MIRV and brightest-blob radial convection velocity to be alike. Simulation and NSTX experimental MIRVs were also found to have similar pdfs and it may be inferred that the fluid convection velocities in NSTX and in the simulation are distributed alike as well.

The ability to make direct, quantitative comparisons between GPI intensity image dynamics measured in simulation

and in experiment has been demonstrated here for the first time. However, we urge caution against inferring exclusive physical explanations for the observed and simulated turbulent phenomena in the SOL. The level of agreement obtained here is satisfying but not definitive. There are physical processes at work in the experiment that likely contribute to the intensity profiles studied here, which, though we have made no attempt to simulate them, may masquerade as a simulated effect. Physics omitted from the present model which may be relevant to boundary turbulence and GPI modeling includes: three-dimensional effects of magnetic geometry and X-points, modeling of divertor plate sheath conditions, flux surface shape and magnetic shear, SOL ionization and radiation, wall recycling, and kinetic effects, which are all outside the scope of the fluid model. Exploration of such topics remains for future research.

ACKNOWLEDGMENTS

We are grateful to B. P. LeBlanc for providing the Thomson scattering data for the NSTX shot.

This work was supported by the U.S. Department of Energy (DOE) under Grant Nos. DE-FG02-02ER54678, DE-FG02-97ER54392, and DE-AC02-09CH11466; however, this support does not constitute an endorsement by the DOE of the views expressed herein.

APPENDIX: ZONAL MOMENTUM AND VORTICITY DYNAMICS FROM CHARGE CONSERVATION

A potentially confusing point of the model equations is the relationship between the fluctuating vorticity equation and the zonal momentum equation. The relationship of these equations is most easily illustrated in the simple limit $\alpha_{\text{dw}} = \beta = \mu = \bar{\mu} = \nu_p = 0$.

We begin with the charge conservation equation balancing the divergences of the perpendicular ion polarization current and the parallel current

$$\nabla \cdot \frac{d}{dt} (n \nabla \Phi) = \alpha_{\text{sh}} n T^{1/2} (1 - e^{(\Phi_B - \Phi)/T}) \quad (\text{A1})$$

where $d/dt = \partial/\partial t + \mathbf{v} \cdot \nabla$ and the right-hand side represents the field-line-integrated term $\nabla_{\parallel} \mathbf{J}_{\parallel}$, i.e., the boundary term describing charge losses to the sheaths. The zonal (i.e., y) average of this equation is

$$\frac{\partial}{\partial x} \left\langle \frac{d}{dt} (n v_y) \right\rangle = \langle \alpha_{\text{sh}} n T^{1/2} (1 - e^{(\Phi_B - \Phi)/T}) \rangle$$

where $\mathbf{v}_y = \partial \Phi / \partial x$. Integrating in x then yields

$$\frac{\partial p_y}{\partial t} + \frac{\partial}{\partial x} \langle n v_x v_y \rangle = - \int_x^{L_x} dx \alpha_{\text{sh}} \langle n T^{1/2} (1 - e^{(\Phi_B - \Phi)/T}) \rangle, \quad (\text{A2})$$

where $p_y = \langle n v_y \rangle$ and some algebraic manipulations were performed for the convective part of d/dt to obtain the density-weighted Reynolds stress term $\langle n v_x v_y \rangle$, as described in more detail in Ref. 27. Note that retention of \mathbf{J}_{\parallel} on closed surfaces (α_{dw}) or of curvature (β) does not modify the zonal momentum equation because terms of the form $\nabla_{\parallel} \mathbf{J}_{\parallel}$ are

annihilated by a zonal (i.e., flux surface) averaging on closed surfaces. Thus we recover Eq. (4) of the main text in the limit $\bar{\mu} = \nu_p = 0$.

On the other hand, the fluctuating part of charge conservation (A1), denoted by $\{\dots\}$ yields, under the Boussinesq (constant density) approximation

$$\left\{ \nabla \cdot \frac{d}{dt} \nabla \Phi \right\} = \{ \alpha_{sh} T^{1/2} (1 - e^{(\Phi_B - \Phi)/T}) \}.$$

Then, after some algebraic manipulations (again on the convective part of d/dt), one obtains

$$\left\{ \frac{d}{dt} \nabla^2 \Phi \right\} = \{ \alpha_{sh} T^{1/2} (1 - e^{(\Phi_B - \Phi)/T}) \}, \quad (\text{A3})$$

which is equivalent to Eq. (3) of the main text in the limit $\alpha_{dw} = \beta = \mu = 0$.

Thus, Eqs. (3) and (4) are simply the y -averaged or “zonal” (A2) and y -varying (A3) parts of the charge conservation Eq. (A1) and they are used to advance $\bar{\Phi}$ and $\tilde{\Phi}$, respectively. In the numerical implementation, once $p_y = \langle n v_y \rangle = \bar{n} \bar{v}_y + \langle \tilde{n} \tilde{v}_y \rangle$, \bar{n} , and $\tilde{\Phi}$ are known at the new time-step, the updated value of $\bar{\Phi}$ is obtained by integration of $\bar{v}_y = \partial \bar{\Phi} / \partial x$. We choose to model the fields $\bar{\Phi}$ and $\tilde{\Phi}$ separately because (i) it is useful to monitor total momentum flux explicitly (e.g., for momentum conservation studies) and (ii) in a tokamak $\tilde{\Phi}$ and p_y are distributed along the field line differently and therefore are potentially subject to different physical dissipations in realistic divertor geometry.

While the equation set used here is explicitly constructed to conserve the proper density-weighted zonal momentum (of interest for the dynamics of zonal flows induced by blob ejection, see Ref. 28), it is not likely to possess an energy theorem. It is readily shown that the system energy takes the form (in dimensionless variables)

$$E = \int d^3x \left(\frac{1}{2} n |\nabla \Phi|^2 + \frac{3}{2} n T \right). \quad (\text{A4})$$

(In the limit $c \gg v_a$, the vacuum electric field energy is negligible and was dropped here.) Consider first the case of pure advection, described by Eq. (A1) with $\alpha_{sh} = 0$, together with $dn/dt = dT/dt = 0$. In this case, it can be shown that both terms in E are conserved separately. Parallel electron dynamics (modeled by α_{dw}) and curvature (modeled by β), when retained to sufficiently high order in *all* equations (vorticity, density and temperature; see, e.g., Ref. 42), preserve the conservation of total E and allow for energy exchange between the two terms. However, the required additional terms in the density and temperature equations are negligible when compared with the sheath loss terms that are essential for modeling SOL physics. Consider, for example, a typical curvature term that results from compressibility effects in the continuity equation. The ratio of the curvature drift frequency to the sheath end-loss rate is $cT / (eB R_{L\perp}) : c_s / L_{\parallel} = L_{\parallel} \rho_s / R L_{\perp}$ which reduces to ρ_s / L_{\perp} if we take $R \sim L_{\parallel}$. Thus, in the fluid limit of these simulations, $\rho_s / L_{\perp} \ll 1$, SOL energetics is dominated by end loss and is fundamentally non-conservative. One might even say that the dominance of end

loss *defines* the SOL. The situation is still more extreme for the temperature equation, where end losses are further enhanced by the sheath energy transmission coefficient $s_E \gg 1$. For this reason, energy conservation is not expected in the SOL and is largely irrelevant for realistic modeling of SOL dynamics.

- ¹S. J. Zweben, J. A. Boedo, O. Grulke, C. Hidalgo, B. LaBombard, R. J. Maqueda, P. Scarin, and J. L. Terry, *Plasma Phys. Controlled Fusion* **49**, S1 (2007).
- ²W. Fundamenski, O. E. Garcia, V. Naulin, R. A. Pitts, A. H. Nielsen, J. J. Rasmussen, J. Horacek, J. P. Graves, and JET EFDA Contributors, *Nucl. Fusion* **47**, 417 (2007).
- ³O. E. Garcia, J. Horacek, R. A. Pitts, A. H. Nielsen, W. Fundamenski, V. Naulin, and J. J. Rasmussen, *Nucl. Fusion* **47**, 667 (2007).
- ⁴O. E. Garcia, R. A. Pitts, J. Horacek, J. Madsen, V. Naulin, A. H. Nielsen, and J. J. Rasmussen, *Plasma Phys. Controlled Fusion* **49**, B47 (2007).
- ⁵R. H. Cohen, B. LaBombard, D. D. Ryutov, J. L. Terry, M. V. Umansky, X. Q. Xu, and S. Zweben, *Nucl. Fusion* **47**, 612 (2007).
- ⁶V. Naulin, T. Windisch, and O. Grulke, *Phys. Plasmas* **15**, 012307 (2008).
- ⁷B. Li, B. N. Rogers, P. Ricci, and K. W. Gentle, *Phys. Plasmas* **16**, 082510 (2009).
- ⁸S. J. Zweben, B. D. Scott, J. L. Terry, B. LaBombard, J. W. Hughes, and D. P. Stotler, *Phys. Plasmas* **16**, 082505 (2009).
- ⁹B. Lipschultz, X. Bonnin, G. Counsell, A. Kallenbach, A. Kukushkin, K. Krieger, A. Leonard, A. Loarte, R. Neu, R. A. Pitts, T. Rognlén, J. Roth, C. Skinner, J. L. Terry, E. Tsitrone, D. Whyte, S. Zweben, N. Asakura, D. Coster, R. Doerner, R. Dux, G. Federici, M. Fenstermacher, W. Fundamenski, P. Ghendrih, A. Herrmann, J. Hu, S. Krasheninnikov, G. Kruemov, A. Kreter, V. Kurnaev, B. LaBombard, S. Lisgo, T. Nakano, N. Ohno, H. D. Pacher, J. Paley, Y. Pan, G. Pautasso, V. Philipps, V. Rohde, D. Rudakov, P. Stangeby, S. Takamura, T. Tanabe, Y. Yang, and S. Zhu, *Nucl. Fusion* **47**, 1189 (2007).
- ¹⁰S. J. Zweben and R. W. Gould, *Nucl. Fusion* **25**, 171 (1985).
- ¹¹S. J. Zweben, R. J. Maqueda, D. P. Stotler, A. Keese, J. Boedo, C. E. Bush, S. M. Kaye, B. LeBlanc, J. L. Lowrance, V. J. Mastrocola, R. Maingi, N. Nishino, G. Renda, D. W. Swain, J. B. Wilgen, and NSTX Team, *Nucl. Fusion* **44**, 134 (2004).
- ¹²J. L. Terry, N. P. Basse, I. Cziegler, M. Greenwald, O. Grulke, B. LaBombard, S. J. Zweben, E. M. Edlund, J. W. Hughes, L. Lin, Y. Lin, M. Porkolab, M. Sampsell, B. Veto, and S. J. Wukitch, *Nucl. Fusion* **45**, 1321 (2005).
- ¹³M. Agostini, P. Scarin, R. Cavazzana, F. Sattin, G. Serianni, M. Spolaore, and N. Vianello, *Plasma Phys. Controlled Fusion* **51**, 105003 (2009).
- ¹⁴N. Ben Ayed, A. Kirk, B. Dudson, S. Tallents, R. G. L. Vann, H. R. Wilson, and MAST Team, *Plasma Phys. Controlled Fusion* **51**, 035016 (2009).
- ¹⁵J. A. Boedo, D. L. Rudakov, R. A. Moyer, G. R. McKee, R. J. Colchin, M. J. Schaffer, P. G. Stangeby, W. P. West, S. L. Allen, T. E. Evans, R. J. Fonck, E. M. Hollmann, S. Krasheninnikov, A. W. Leonard, W. Nevins, M. A. Mahdavi, G. D. Porter, G. R. Tynan, D. G. Whyte, and X. Q. Xu, *Phys. Plasmas* **10**, 1670 (2003).
- ¹⁶B. Nold, G. D. Conway, T. Happel, H. W. Muller, M. Ramisch, V. Rohde, U. Stroth, and ASDEX Upgrade Team, *Plasma Phys. Controlled Fusion* **52**, 065005 (2010).
- ¹⁷R. J. Maqueda, D. P. Stotler, and NSTX Team, *Nucl. Fusion* **50**, 075002 (2010).
- ¹⁸S. H. Müller, A. Diallo, A. Fasoli, I. Furno, B. Labit, and M. Podestà, *Phys. Plasmas* **14**, 110704 (2007).
- ¹⁹G. S. Xu, V. Naulin, W. Fundamenski, C. Hidalgo, J. A. Alonso, C. Silva, B. Goncalves, A. H. Nielsen, J. Juul Rasmussen, S. I. Krasheninnikov, B. N. Wan, M. Stamp, and JET EFDA Contributors, *Nucl. Fusion* **49**, 092002 (2009).
- ²⁰S. I. Krasheninnikov, D. A. D'Ippolito, and J. R. Myra, *J. Plasma Phys.* **74**, 679 (2008).
- ²¹O. E. Garcia, *J. Plasma Fusion Res.* **4**, 019 (2009).
- ²²R. J. Maqueda, G. A. Wurden, D. P. Stotler, S. J. Zweben, B. LaBombard, J. L. Terry, J. L. Lowrance, V. J. Mastrocola, G. F. Renda, D. A. D'Ippolito, J. R. Myra, and N. Nishino, *Rev. Sci. Instrum.* **74**, 2020 (2003).

- ²³J. R. Myra, D. A. D'Ippolito, D. P. Stotler, S. J. Zweben, B. P. LeBlanc, J. E. Menard, R. J. Maqueda, and J. Boedo, *Phys. Plasmas* **13**, 092509 (2006).
- ²⁴T. Munsat and S. J. Zweben, *Rev. Sci. Instrum.* **77**, 103501 (2006).
- ²⁵M. Ono, S. M. Kaye, Y.-K. M. Peng, G. Barnes, W. Blanchard, M. D. Carter, J. Chrzanowski, L. Dudek, R. Ewig, D. Gates, R. E. Hatcher, T. Jarboe, S. C. Jardin, D. Johnson, R. Kaita, M. Kalish, C. E. Kessel, H. W. Kugel, R. Maingi, R. Majeski, J. Manickam, B. McCormack, J. Menard, D. Mueller, B. A. Nelson, B. E. Nelson, C. Neumeyer, G. Oliaro, F. Paoletti, R. Parsells, E. Perry, N. Pomphrey, S. Ramakrishnan, R. Raman, G. Rewoldt, J. Robinson, A. L. Roquemore, P. Ryan, S. Sabbagh, D. Swain, E. J. Synakowski, M. Viola, M. Williams, J. R. Wilson, and NSTX Team, *Nucl. Fusion* **40**, 557 (2000).
- ²⁶J. R. Myra, D. A. Russell, D. A. D'Ippolito, J.-W. Ahn, R. Maingi, R. J. Maqueda, J. Boedo, D. P. Lundberg, D. P. Stotler, S. J. Zweben, and M. Umansky, *Phys. Plasmas* **18**, 012305 (2011).
- ²⁷D. A. Russell, J. R. Myra, and D. A. D'Ippolito, *Phys. Plasmas* **16**, 122304 (2009).
- ²⁸J. R. Myra, D. A. Russell, and D. A. D'Ippolito, *Phys. Plasmas* **15**, 032304 (2008).
- ²⁹G. L. Falchetto, Y. Sarazin, X. Garbet, Ph. Ghendrih, M. Ottaviani, S. Benkadda, and P. Beyer, Proceedings of the 20th IAEA Fusion Energy Conference, 1–6 November 2004, Vilamoura, Portugal, Paper No. TH/1-3Rd.
- ³⁰M. Wakatani and A. Hasegawa, *Phys. Fluids* **27**, 611 (1984); A. Hasegawa and M. Wakatani, *Phys. Rev. Lett.* **59**, 1581 (1987).
- ³¹N. Bisai, A. Das, S. Deshpande, R. Jha, P. Kaw, A. Sen, and R. Singh, *Phys. Plasmas* **12**, 072520 (2005); **12**, 102515 (2005).
- ³²O. E. Garcia, J. Horacek, R. A. Pitts, A. H. Nielsen, W. Fundamenski, J. P. Graves, V. Naulin, and J. Juul Rasmussen, *Plasma Phys. Controlled Fusion* **48**, L1 (2006).
- ³³Skewness measures asymmetry in the distribution of fluctuations about the mean $S_p = \langle (\delta p)^3 \rangle / \langle (\delta p)^2 \rangle^{3/2}$, $\delta p = p - \langle p \rangle$.
- ³⁴D. A. Russell, J. R. Myra, and D. A. D'Ippolito, *Phys. Plasmas* **14**, 102307 (2007).
- ³⁵O. Grulke, J. L. Terry, B. LaBombard, and S. J. Zweben, *Phys. Plasmas* **13**, 012306 (2006).
- ³⁶D. P. Stotler, J. Boedo, B. LeBlanc, R. J. Maqueda, and S. J. Zweben, *J. Nucl. Mater.* **363–365**, 686 (2007).
- ³⁷J. R. Myra, D. A. D'Ippolito, S. I. Krasheninnikov, and G. Q. Yu, *Phys. Plasmas* **11**, 4267 (2004).
- ³⁸The full width-at-half-maximum of the blob in the poloidal dimension is $a \cdot 2[2 \ln(2)]^{1/2} \cong a \cdot 2.36$; a is the "radius of the blob."
- ³⁹D. A. D'Ippolito, J. R. Myra, S. I. Krasheninnikov, G. Q. Yu, and A. Y. Pigarov, *Contrib. Plasma Phys.* **44**, 205 (2004).
- ⁴⁰S. Oldenbürger, C. Brandt, F. Brochard, N. Lemoine, and G. Bonhomme, *Rev. Sci. Instrum.* **81**, 063505 (2010).
- ⁴¹S. J. Zweben, *Bull. Am. Phys. Soc.* **55**, 149 (2010), paper JI2-3; Y. Sechrest, T. Munsat, D. A. D'Ippolito, R. J. Maqueda, J. R. Myra, D. Russell, and S. J. Zweben, *Phys. Plasmas* **18**, 012502 (2011).
- ⁴²J. F. Drake and T. M. Antonsen, *Phys. Fluids* **27**, 898 (1984).